Theoretical and experimental study of direct contact membrane distillation

Isam Janajreh*, Dana Suwwan, Raed Hashaikeh

Mechanical and Materials Engineering Department, Masdar Institute of Science and Technology, P.O. Box 54224, Abu Dhabi, UAE, emails: ijanajreh@masdar.ac.ae (I. Janajreh), dsuwwan@masdar.ac.ae (D. Suwwan), rhashaikeh@masdar.ac.ae (R. Hashaikeh)

ABSTRACT

Direct contact membrane distillation (DCMD) is characterized as a low-thermal energy process, involving evaporation and a phase change driven by the pressure difference between two fluid channels separated by a hydrophobic membrane. The temperature difference creates a driving pressure between the hot channel (feed) and the cold channel (permeate). This paper demonstrates the performance of the DCMD through high fidelity simulation and experimental observation to reveal a fundamental and qualitative understanding of the spatial distribution of the temperature, mass flux, and heat flux as well as the temperature polarization. The flow model is governed by the Navier–Stokes equations of non-isothermal fluid coupled with the energy equation for the two adjacent channel flow and the middle hydrophobic and porous membrane. The experimental study involved the development of a transparent acrylic DCMD unit operated by two peristaltic pumps where each cycles the feed and the permeate from the corresponding reservoir through the DCMD chambers that are separated by the PVDF–HFP membrane. The hot feed reservoir temperature is maintained at 40°C (4% salinity), whereas the permeate reservoir temperature is kept at 25°C (0% salinity). The system is tested using membranes of prescribed thickness, porosity, and conductivity. The model and experimental results were compared in counterflow configurations and a good agreement between the model and experimental was obtained for temperature distributions, mass flux, and temperature polarization coefficient (TPC). The system metrics were obtained for the DCMD showing a suitable TPC working range (0.3–0.55), a relatively low mass flux yield (5 kg/h m^2) and a very low thermal efficiency (1.5%). These results suggest there is still a large potential in DCMD to enhance its overall yield in order to speed up their large-scale commercialization.

Keywords: Mass transfer; Heat transfer; Temperature polarization coefficient (TPC); Hydrophobic

1. Introduction

Membrane distillation (MD) is a low-grade energy demanding process. It could be applied in the desalination industry qualifying it to be more attractive and economically feasible in comparison to other techniques or other thermal desalination, i.e. reverse osmosis and multistage flash [1–3]. Direct contact membrane distillation (DCMD) is receiving immense

*Corresponding author.

academic interest [4] because of the simplicity in configuration (Fig. 1), flexibility in scaling up, and its outstanding rejection performance that can reach as high as 100% [5–7]. The mechanism is comprised of two channel flows separated by a thin porous hydrophobic membrane. The streams are mainly a hot brine solution and cold freshwater, commonly referred to as feed and permeate, respectively. The involved physics is a combined evaporation, transportation of mass and heat flux through the permeable membrane and condensation of the permeated vapor. The presence of the two flows at different temperatures across the thin porous membrane creates a pressure difference. This also results in a localized evaporation at the hot membrane side and the potential transport to the cooler permeate side through the membrane micropores. The induced pressure gradient facilitates the flow of vapor through the membrane pores before it condenses at the permeate side where the flux is collected. This distillation process involves three stages: firstly, evaporation of feed side; secondly, conduction through the pores; finally, condensation at the permeate side. Many simulations have been conducted in the process of enhancing the DCMD configurations with the primary objective to estimate the permeate flux and its dependence on the membrane parameters and operating variables [8]. Generally, the same author pointed out that the reported DCMD work adapted the classical experimentation method, i.e. single parametric study which is time consuming without parametrical interaction effect leading to inefficient optimization. Modeling of the channel flow poses no technical issues, whereas flow evaporation and transport in porous media are technically very challenging.

In this work, neither the evaporation nor the flow within a porous media is explicitly modeled, but rather the computed temperature is utilized to evaluate the saturation pressure using a tabulated thermodynamic pressure–temperature relationship. This work also skips the lengthy functional correlations to estimate the thermal boundary layer parameters (Nusselt, Prandtl, Reynold, Shmidt, and Sherwood numbers) appear elsewhere [9], as it is been resolved directly within the framework of a coupled conjugated heat flow under the implementation of a high-resolution discretization mesh. The transport phenomenon within the porous membrane is accounted for by implementing the Poiseiulle and Knudsen flow model that has appeared in several literature work [4,6–10].

Other published works that assess the impacts of parameters affecting the yield of the system are found in [4,6,11,12] et al. Some studies have considered the microscopic membrane properties and fabrication processes [13,14], while others were devoted to molecular dynamics and simulations as well as the development of fundamental interactions between liquid–liquid and solid–liquid encountered in phase change [15,16]. On the other hand, macro-level studies were conducted on varying flow and inlet conditions and their effects on the system performance. Previously, the author conducted studies incorporating the integration of spacers and studied their impact on the heat and mass fluxes [17] as system output. Furthermore, turbulence was thought to improve the yield due to the addition of spacers that modify the thermal boundary layer and lead to a larger temperature polarization (the ratio of the cross-membrane surface temperature to that of the bulk temperature), thereby leading to a better yield of the system [18–20].

Additionally, modeling the problem as a conjugated heat transfer was previously conducted by the author and a few others [17,21–23]. These studies involved models applicable for counter and parallel flow configurations in which several inlet conditions such as temperature, velocity, and membrane characteristics were investigated. Also, authors in [10,24–29] et al. integrated the theoretical model predictions with the establishment of experimental work in an attempt to develop a comprehensive analysis and address the comparisons. These models not only lack the modeling details, but also consider strong assumptions such as a completely insulated system, lack of mass flux coefficient dependency on the evaluated temperatures, and similar feed and permeate water properties.

This paper intends to develop a robust-conjugated heat flow model that accounts for the different flow properties (viscosities and densities) to investigate and validate the flow within the context of DCMD and to quantify process performance metrics. The developed model is intended to be generic in order to assess the DCMD performance under different flow configurations, various flow materials and properties, and to accommodate different membrane physical properties. The model is developed based on computational fluid dynamics (CFD) and is deployed as a design tool in MD applied to desalination, juice concentration, oil–water separation, or even medicinal application. The governing Navier–Stokes flow coupled with energy is modeled in this work and the model can be used in planer or in cylindrical configuration. e. This work also involved the development of an experimental DCMD test unit to serve as a test bed and practical validation/tuning tool to accommodate a broader application. In the context of water desalination, the validation of the model was conducted in terms of temperature distributions, temperature polarization coefficient (TPC), and mass flux of the system.
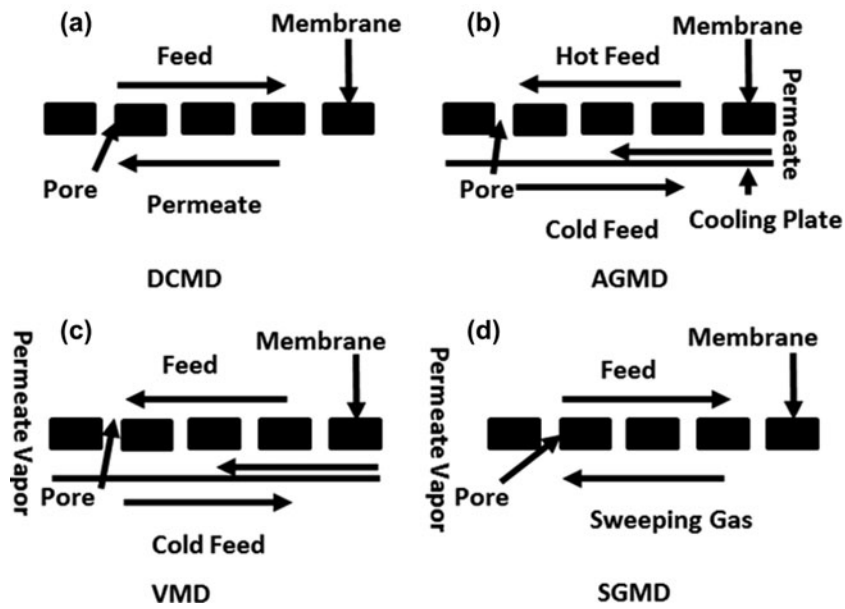
Fig. 1. Different configurations of MD.

The right implementation of the analysis is expected to reveal the current metrics and what the targeted parameters are to bring this technology a step closer to economic and feasible commercialization.

2. Model development

2.1. Governing flow equations

The flow within the enclosed DCMD unit consisting of the membrane, feed, and permeate chambers is schematically depicted in Fig. 2. It is governed by the viscous, incompressible non-isothermal flow which is governed by the mass conservation (Eq. (1)) and Navier–Stokes/momentum (Eqs. (2) and (3)) and are coupled with the energy (Eq. (4)). These equations are written as:

Fig. 2. Schematic diagram of the DCMD parallel flow.

$$\frac{\partial \rho}{\partial t} + \frac{\partial (\rho u)}{\partial x} + \frac{\partial (\rho v)}{\partial y} = 0 \tag{1}$$

$$\frac{\partial (\rho u)}{\partial t} + u\frac{\partial (\rho u)}{\partial x} + v\frac{\partial (\rho u)}{\partial y} = -\frac{\partial (p)}{\partial x} + \mu\left(\frac{\partial^2 u}{\partial x^2} + \frac{\partial^2 u}{\partial y^2}\right) \tag{2}$$

$$\frac{\partial (\rho v)}{\partial t} + u\frac{\partial (\rho v)}{\partial x} + v\frac{\partial (\rho v)}{\partial y} = -\frac{\partial (p)}{\partial y} + \mu\left(\frac{\partial^2 v}{\partial x^2} + \frac{\partial^2 v}{\partial y^2}\right) + \rho g_y \tag{3}$$

where ρ is the fluid density, u and v are, respectively, the axial and transversal velocity components, p is the hydrodynamic pressure and μ is the molecular viscosity, and g is the gravitational acceleration.

The scalar energy equation is also given by:

$$\frac{\partial \rho C_p T}{\partial t} + u\frac{\partial \rho C_p T}{\partial x} + v\frac{\partial \rho C_p T}{\partial y} = k\left(\frac{\partial^2 T}{\partial x^2} + \frac{\partial^2 T}{\partial y^2}\right) + S_h \tag{4}$$

where C_p is the specific heat, T is the temperature, and k is the medium thermal conductivity. The S_h is any additional external heat source or losses. The resolution of these equations provides the u and v velocities, along with temperature and pressure in the entire flow field in Fig. 2 and when the domain is subjected
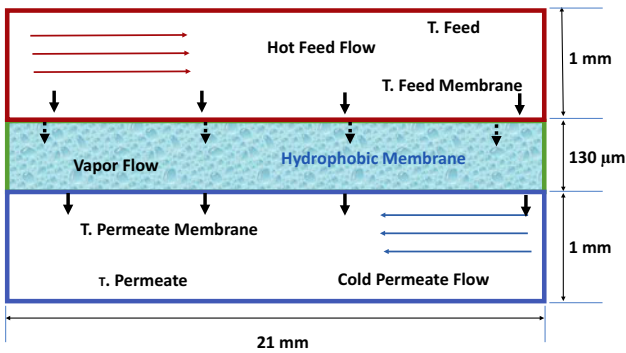
to the proper inlet and outflow velocity and temperature conditions that correspond to the feed, permeate pump flow rates, and reservoir temperatures.

2.2. Flow properties and boundary conditions

The model dimension schematics for DCMD are depicted in Fig. 2. The figure displays two stream channels in an adjacent and parallel configuration. As the relatively hot feed stream enters, it is subjected to localized vaporization due to its low partial pressure, which starts to diffuse through the hydrophobic membrane pore. Vapor is transported through the pores by means of convection where condensation occurs at the permeate collection side. Optimization of the DCMD depends on several flow conditions such as temperature and velocity as well as membrane properties such as porosity, tortuosity thermal conductivity, and thickness [4,11,12].

For this particular model development, several assumptions were taken into consideration. The considered model is two dimensional prescribed in a Cartesian x and y coordinates, i.e. axially in x, vertically cross the channel in y direction. A steady state flow is assumed and incompressible non-isothermal flow. The zero velocity (no slip) condition and adiabatic conditions are applied to the outer channel walls because a flexible Styrofoam thermal insulation is used to cover the destination unit and running hoses in order to minimize convectional heat losses. The flow is considered fully developed (since vertical height is far less than horizontal length) and the flows are of single species. The no-penetration condition is used at either side of the membrane as the amount is very small compared to the transported channel flow. The transmembrane mass flow is calculated according to the Knudson and Poiseuille flow model as was reported by several authors [10,21–24,27].

2.3. Numerical model development

The model is based on Fig. 2 and in phase with previous numerical simulation studies within the context of DCMD of the authors. A discretized mesh of the two-channel flow, conjugated with the solid membrane thermal performance, represents the physical domain. The mesh is made of high-quality structured quadrilateral cell type for the feed, permeate, and the membrane. The domain is comprised of 400×40 cells in each channel, and 400×12 for the membrane, totaling 36,800 that are clustered near the wall to capture the thermal and kinetic boundary layers. Inlet and wall Dirichlet conditions (prescribed velocity and temperature value) and outlet Neumann conditions (zero

gradients) are applied. The system walls are associated with no slip and no penetrating velocity, coupled membrane wall surface temperature and adiabatic thermal conditions are applied to the outer channel. A cutaway of the baseline mesh and the computational domain boundary conditions are depicted in Fig. 3.

2.4. Process metrics

2.4.1. Total mass flux

In the DCMD process, evaluating the transport of mass constitutes the process productivity. Due to the temperature gradient, a driving pressure force is created which is responsible for the mass transfer across the membrane [7]. The general form of the mass flux is illustrated by Chen and Greenlee [5,7], and is written as:

$$J'' = c_m(P_f^{\text{sat}} - P_p^{\text{sat}}) \tag{5}$$

It equates to the multiple of the mass coefficient (c_m) and the cross-membrane saturation pressure (P^{sat}) gradients. The c_m is obtained from either of the models, namely Knudson diffusion, molecular diffusion, Poiseuille flow, or Monte Carlo as reported by Ding in [30], Bui et al. [31] and Imdakum and Mussarra [32]. The pressure is linked to the computed temperature value from the flow model.

The transmembrane heat flux is described by the latent heat flux and conduction through the membrane that is created by the temperature gradient across the membrane. This temperature creates the saturation pressure that steers the flow through the membrane. This pressure is computed from thermodynamic tables
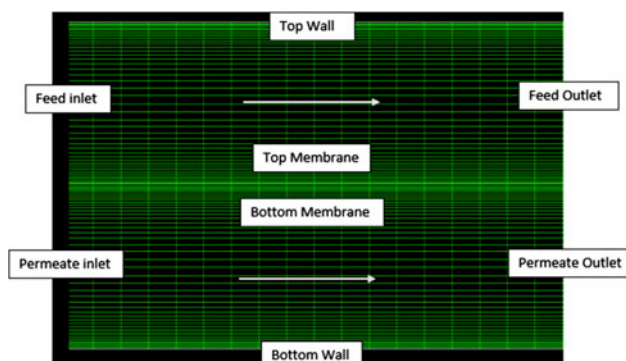

Fig. 3. Numerical DCMD mesh model subjected to specific inlet and boundary conditions (thickness is exploded by 50 times to show the mesh).

or according to Antoine's equation within the applied temperature range as [33]:

$$P_{i(\text{pure})}^{\text{sat}} = \exp\left(23.238 - \frac{3841}{T - 45}\right), \quad i \in \{f, p\} \tag{6}$$

A suitable combination of Knudson (c_k) and Poiseuille (c_p) coefficient models is used in this work. This model shows its consistency in evaluating the mass flux as was presented by Chen [7]. Accordingly, the mass flux coefficient is expressed as:

$$\begin{aligned} c_m &= c_k + c_p \\ &= 1.064\alpha(T)\frac{\varepsilon r_p}{\tau\delta_m}\sqrt{\frac{M_m}{RT_m}} + 0.125B(T)\frac{\varepsilon r_p^2}{\tau\delta_m}\frac{M_m P_m}{RT_m \mu} \end{aligned} \tag{7}$$

where ε, r_p, τ, and δ are, respectively, the porosity, average pour radius, tourtuisity, and membrane thickness. T_m and P_m are the average spatial temperature and pressure, respectively, and R is the universal gas constant. It should be emphasized that while ε, r_p, τ, δ, and the fluid molecular wight (M_w) are membrane or fluid-dependent properties, the spatial average membrane temperature (T_m) and the average spatial pressure (P_m) are functions of the computed pressure and temperature which are strongly coupled to the flow.

2.4.2. Heat flux

The heat transfer in the DCMD process can be described following three steps: the heat transfer through the feed boundary layer, heat transfer through membrane, and heat transfer through the permeate boundary layer [10]. The total heat flux for the membrane is due to the convection through the feed membrane surface which is equated to the convection through the permeate membrane surface, and that is also equated to the combined conduction (Q_m) and latten heat of evaporation through the membrane. An illustration of the heat transfer pathways in the form of the electrical resistances analogy is given in Fig. 4. The heat conduction across the membrane material is in part due to the bulk membrane material conduction (Q_c) and to the vapor-filled pores (Q_v). The total membrane heat flux can be described as:
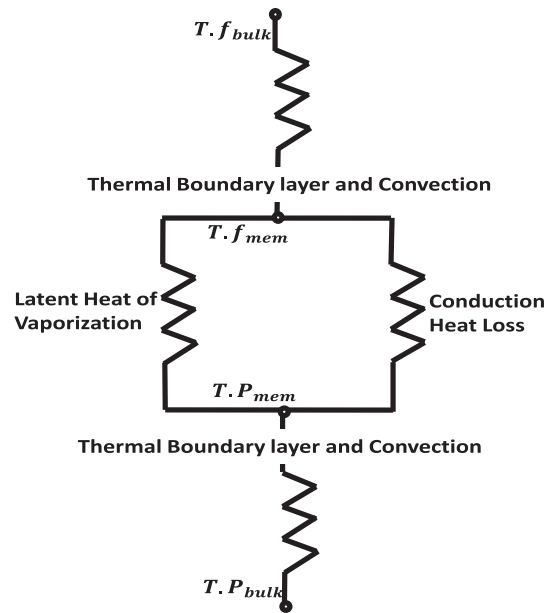
$$Q_m = Q_c + Q_v \tag{8}$$

Fig. 4. Heat transfer resistances associated with DCMD.

The transmembrane heat flux is written as:

$$Q_v = J''\Delta H = J''(H_{m,f} - H_{m,p}) \tag{9}$$

ΔH here is the latent heat of the transmembrane flux of the fluid and $H_{m,f}$ and $H_{m,p}$ signify the latent heat of the feed and the permeate, respectively. According to Termpiayakul [32], it is equated to enthalpy which can be found from the saturated water vapor and liquid thermodynamic charts. The conduction is expressed according to Fourier law as:

$$Q_c = -\frac{k_m}{\delta_m}\left(T_{m,f} - T_{m,p}\right) \tag{10}$$

where the total conductivity coefficient (k_m) is evaluated according to the void or porosity of the membrane and is based on the volume weighted average of the bulk conductivity (k_b) and the vapor conductivity (k_g). This conductivity is expressed as:

$$k_m = \varepsilon k_g + (1 - \varepsilon)k_b \tag{11}$$

2.4.3. DCMD thermal efficiency (η)

This metric is governed by the fraction of the heat used as latent heat of evaporation instead of the lost

conduction fraction. This efficiency can be represented as:

$$\eta = J'' \Delta H_m / Q_m \tag{12}$$

where Q_m is the total transmembrane heat which is a combination between the latent heat of evaporations by a small margin and the thin membrane conduction. This can be described as:

$$Q_m = J'' \Delta H_m + k_m \left(T_{mf} - T_{mp} \right) / \delta_m \tag{13}$$

Lower membrane conductivity contributes to the increase in the thermal efficiency by providing a better chance to accumulate a larger share of latent evaporation heat instead of the non-contributing mass flux of the conductive heat.

2.4.4. Temperature polarization coefficient-TPC or (θ)

It measures the ratio of boundary layer resistance over the total heat transfer resistance, and mathematically is the ratio of the cross-membrane temperature difference to that of the bulk temperature difference and is written as:

$$\theta = \frac{T_{m,f} - T_{m,p}}{T_{b,f} - T_{b,p}} = \frac{\Delta T_m}{\Delta T_b} \tag{14}$$

For small θ (≤ 0.3), the DCMD is considered heat transfer limited implying the module design is poor, i.e. highly conductive or extremely thin membrane that generates a low operating temperature difference. For larger θ value (≥ 0.6), the DCMD enters the mass transfer limitation. It is hindered because of constraining membrane permeability [34]. Therefore high TPC operation membrane needs to be at high permeability, but also high tortuosity to ensure product and rejection quality.

3. Experimental Setup

3.1. Development of the DCMD unit

Fig. 5. depicts the developed DCMD cell unit, which is made of two transparent acrylic blocks (30.0 cm × 16.4 cm × 3.1 cm), both precisely milled forming two identical rectangular channels of 21-cm length having 15-cm width and 1-mm depth. The ends of the channels are also precisely machined which ensures a uniform and laminar inlet flow driven by the peristaltic pump. The two machined blocks are characterized with two axes of symmetry as depicted in Fig. 5. The two channels are formed by housing the membrane which is sealed by appropriate rectangular rubber and using 8 butterfly bolt nuts with a 1-cm diameter. The unit dimensions are listed in Table 1.

The schematic and the corresponding experimental setup of the DCMD system setup of seawater desalination are depicted in Fig. 6. Additionally to the DCMD assembly block, it consists of two main reservoir tanks that provide the feed and permeate solutions. The permeate reservoir is used as a thermal well and keeps the least amount of circulated permeate flow within the submerged 1,000-ml flask. The overflow of the flask represents the system mass flux yield overflow into a graduated cylinder that precisely measures the desalinated mass flux yield. The main components of the system setup are listed in Tables 2 and 3.

In order to gain an in-depth insight into the temperature distributions in the channels, and for the module validation, T-type thermocouples were mounted within the two-channel flow to measure the membrane surface temperatures at the zero depth of each block (upper and lower channels surfaces) and 1-mm depth (membrane surfaces). There were twelve thermocouples used within the desalination compartment with, six each side, three of which are to record the membrane surface temperature, while the other three to record the channel surface temperature. Additionally, two other thermocouples are used for temperature measurements of the two reservoirs. The installations enable one to carry a direct comparison of the measured TPC values against the simulation results at a high spatial resolution along the channel. The locations of these installed thermocouples are depicted in Fig. 7. Table 4 lists their designations.

All thermocouples are initially calibrated to insure their linear response or for any needed adjustments in the recorded data. It was conducted using standard heating pads, beaker, and mercury read out thermometer covering a 20–100°C range at 5°C degree increments. All thermocouples showed a well-behaved trend that is zero offset and linear trends at 0.99 regression coefficient. The adopted measurement procedures during the course of experiment following the calibration are as follows:

(1) Setup the feed and permeate temperature thermostats and ensure the salinity value of the feed.
(2) Ensure the permeate overflowing flask is completely full.
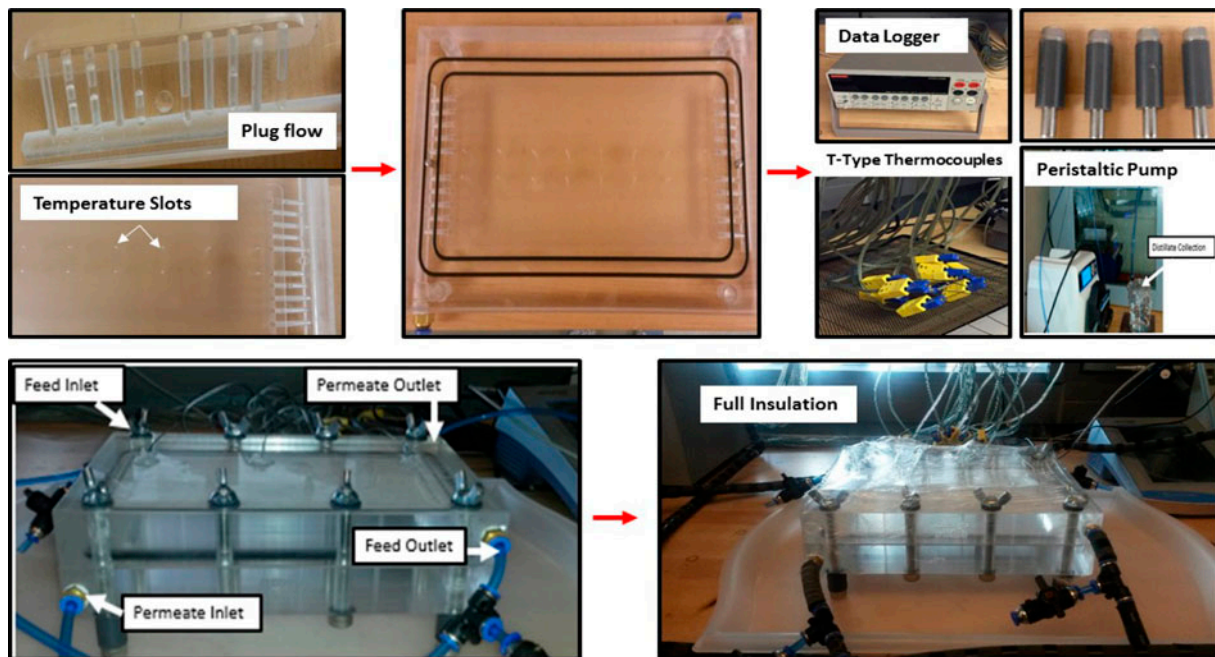(3) Setup the desired pump flow rate (inlet flow velocity or Re = 100).

Fig. 5. Drawings and the fabricated DCMD cell unit.

Table 1
Model dimensions and flow conditions

Unit parameters	Value
Unit length (mm)	300
Unit thickness (mm)	62
Unit width (mm)	164
Channel length (mm)	210
Channel width (mm)	100
Channel height (mm)	1
Membrane effective area (m^2)	0.021
Thermocouple diameter (mm)	1

(4) Measure and record the salinity of the feed and permeate at the start.
(5) Record the temperature at the stipulating sampling rate (1 Hz).
(6) Evaluate the mass flux and salt rejection.

These procedures are illustrated in sequential order in a flowchart as depicted in Fig. 8.

4. Results and discussions

Table 5 shows the experimental conditions where each peristaltic pump flow rate was set to 0.1 l/min equivalent to Reynolds number of 100. Because the cross-sectional area of the tubing is nearly half the entry area of the experimental unit, the Re within

the unit is 50. The counterflow configuration is used as it is more efficient in exchanging heat than the parallel flow, thereby has the potential to produce a higher desalinated mass flux.

The flow initially passes through transient stage as the inlet temperature of the feed as well as the permeate ramped up and adjusted to the stipulated entry flow temperatures. This stage takes nearly one hour in the current setup, however it depends on the system insulation including the unit and the tubing. A well-insulated system will reach a faster steady state, and thereby the resulted mass flux and other metrics tend to be more steady and uniform. Fig. 9 shows the temporal evolution of the temperatures for the reservoir channels (feed 101 and permeate 108). It shows a stable reservoir temperature as these thermal wells are operated in a well-controlled PLC heating stirrer thermostat circuit. The temperatures of the upstream, midstream, and downstream locations at the channel walls for the fee and permeate are also depicted in Fig. 9. Following the initiation phase of nearly one hour, the trend of the temperature tends to be stabilized despite the unnoticed slight increase in the permeate temperature which can be attributed to the thermal conduction of the acrylic unit materials. Similarly, the temperature of the membrane surfaces are captured at the same locations (up, middle, and downstream) which also shows a similar trend following an initial ramp up then stable and fixed values as
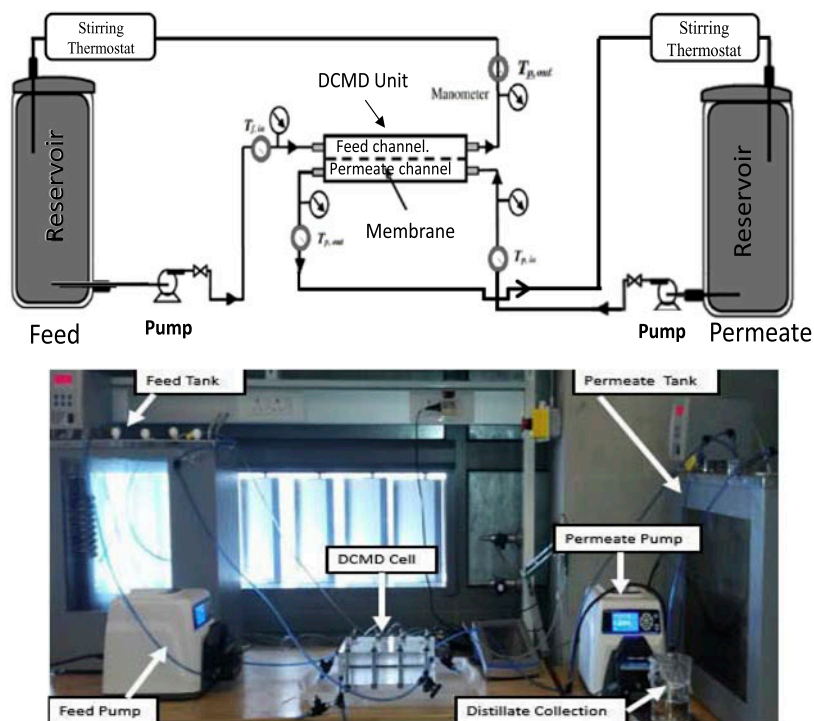
Fig. 6. DCMD schematic and corresponding experimental setup showing the additional permeate overflow into graduated cylinder.

Table 2
List of the components incorporated in the experimental unit

Parts	Quantity	Specification
Machined acrylic blocks	2	Transparent
Hydrophobic membrane	Whole sheet	PVDF–HFP [35], 197-μm thickness, 0.2 w/m k conductivity, 42.27 Psi, liquid entry pressure, 0.15–0.2-μm pore size, electrospinning technology
Pumps	2	Peristaltic
Thermocouples	14	TMQSS-040U-12
Butterfly tie bolts	8	Stainless steel
Polymeric plumping elbows	14	90˚
Reservoir tanks (40L capacity)	2	Electric heater type
Overflow flask	1	Graduated cylinder (1,000 mL)
Mass balance	1	Electronic Max-3,000 g
Salinity and pH indicator	1	Accumet excel XL60 dual channel: pH /ion/salinity/conductivity/Do meter

depicted and compared in Fig. 10 along the feed and permeate temperature reservoirs. The membrane surface temperatures are at lower values than the corresponding wall locations at the feed side and at higher temperature values than the corresponding permeate wall locations as clearly shown in Figs. 9 and 10. It should be emphasized that the data have shown good reproducibility in each run over the course of several days. The relative deviation error remained very small and within ±1.2% in the temperature for each channel following the 60-min induction period (Table 6).

The measured steady state temperature and the evaluated TPC value and its third degree trend line fittings are depicted in Fig. 11. As the hot feed is

Table 3
Thermocouple channel locations and installation

Location	Channel designations
Feed tank	101
Permeate tank	108
Feed wall (0, 72, 168 mm)	102, 103, 104
Feed memb. (0, 72, 168 mm)	202, 203, 204
Permt. memb. (0, 72, 168 mm)	205, 206, 207
Permt. wall (0, 72, 168 mm)	105, 106, 107

injected from left to right, a smaller measured temperature difference of 1.5℃ across the channel is obtained at the feed entry. This difference, however, continues to grow at the middle and downstream reaching nearly 5℃ at the exit of the feed channel. Similarly, at the permeate side following from right to the left, it demonstrates a smaller and nearly equal temperature difference at the entry growing to 5℃ at the permeate channel exit. A key performance metric of the unit is the TPC value along its channel. The obtained value is within the stipulated range {0.35, 0.51} which is below the mass limit (≥0.6) and above the heat limit (≤0.3) operation as indicated by Chen and Ho [7]. A very high TPC value can be associated with wetting and fouling of the membrane which deteriorates the permeated water quality, while a low TPC value implies little thermal potential across the membrane to drive the flow which can be attributed to high membrane conductivity or an extremely slow-moving flow [20]. The obtained TPC values nearly follow the expected symmetrical profile for the counterflow configuration, where the maximum values are localized at the flow entry and are attributed to largest membrane temperature potential as shown in Fig. 11.

Results of the model values that are based on conjugated heat transfer flow that couples the membrane thermal properties and flow field are depicted in Fig. 12. The model is subjected to the same entry conditions as listed in Table 1 (i.e. Re = 50 for entry flow,

feed, and permeate temperatures are 40 and 25℃, respectively, and adiabatic conditions at the other channel walls).

Comparison of the experimental and model temperatures and TPC values are shown in Figs. 13 and 14, respectively. The temperature and TPC trends comply with the experimental measurements. The measured temperature at the entry is well behaved as it nearly folds on the obtained model temperature values. However, it starts to deviate from the model entry and onwards particularly at the outer channel wall surfaces as shown at the middle and downstream. This is attributed to the restrictive adiabatic conditions imposed on these walls for the feed and permeate channels that ban heat transfer to the lower ambient/room temperature of 23℃, therefore resulting in higher upper model wall temperature than the actual experimental value. Because similar adiabatic conditions are applied on the lower wall, the amount of heat transfer from the system is also restricted and leads to lower attained temperature values compared to what would incur experimentally. Nevertheless, the obtained model membrane surface temperatures are better behaved when compared to the experimental values which are attributed to the direct and unrestricted thermal flow coupling.

The TPC model values are also compared to the measured experimental values as shown in Fig. 14, which depicts a discrepancy value range of {0.04, 0.095}. It is in favor of the experimental data as the denominator of the TPC, and is fairly overestimated in the model by the imposed adiabatic outer wall conditions. The obtained values, however, are within the stipulated and favorable range {0.3–0.6} suggesting a reasonable model yield without entering the heat transfer or mass transfer system limitations. In general, the TPC as well as the corresponding mass flux decrease spatially due to the development of the boundary layer [22,36–38]. It is clearly demonstrated in the flow as one follows the entry until midstream, that this trend is more obvious in parallel flow
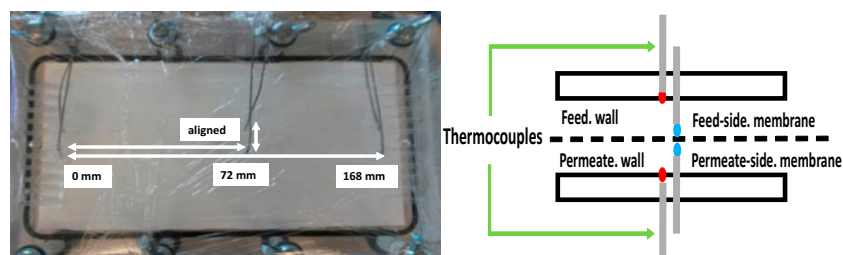

Fig. 7. Thermocouple alignments and designation.

Table 4
Feed and permeate reservoir dimensions and inlet conditions

Dimensions	Feed tank	Permeate flask
Height (m)	0.43	
Length (m)	0.5	1,000 mL
Width (m)	0.2	
Total mass (kg)	43	1.336
Salinity (ppt)	36	0.05

Table 5
Inlet conditions for experimental procedure

Parameter	Value
Pump flow rates (liters/min)	0.1 (Re = 100)
Axial inlet channel velocity (m/s)	0.01718
Feed inlet temperature (°C)	40
Permeate inlet temperature (°C)	25

configuration as it covers the whole stream following the entry point.

The evaluated transmembrane mass flux along the channel length based on the computed membrane surface temperature and the mass flux based on the experimental measurements of the temperatures is

depicted in Fig. 15. The mass flux trend complies with the general norm of the TCP as it reduces in the mid-stream due to lower cross-membrane temperature and increases at the entry points coinciding with a high temperature difference. It is worth mentioning that even though the experimentally evaluated TCP value is clearly higher than the modeled value, the mass flux does not necessarily abide by this trend as it is mainly driven by the cross-membrane temperature difference according to Eq. (5). Moreover, the average mass flux across the membrane is also measured over the course of two hours beyond the initiation/transient period (one-hour period according to Fig. 9). These data are summarized in Table 6.

It can be inferred that the computed model mass flux is lower than the experimentally modeled data that are based on temperature difference, while both experimentally modeled mass flux and the actual measured mass flux have a slight discrepancy. This can include two main points; Firstly, an accurate capture of the temperature distribution will lead to a good estimate of the mass flux as indicated by the thermo-couple temperature data which observed a deviation of only 1.75%; secondly, the Knudson and Poiseuille models are fairly accurate model for mass flux evaluation assuming an accurate temperature date have been accurately evaluated. The deviation in the mass flux model simulation (14.5%) is attributed to the accuracy of the evaluated temperature rather than the Knudson and Poiseuille model. Thus, taking into account this conditional difference, it is fair to conclude that these comparisons serve as a tool to obtain deeper insight into the actual differences hindered by each aspect of mass flux modeling.

Finally, the spatial distribution of the thermal efficiency of the DCMD unit under the current setup and flow conditions is depicted in Fig. 16. It clearly demonstrates the same trend as the mass flux, but also highlights the low DCMD process efficiency. Therefore, great research opportunities present themselves today to increase this efficiency, either by optimizing the flow conditions or by means of an innovative membrane technology. The currently developed model is amenable to accommodate either of these
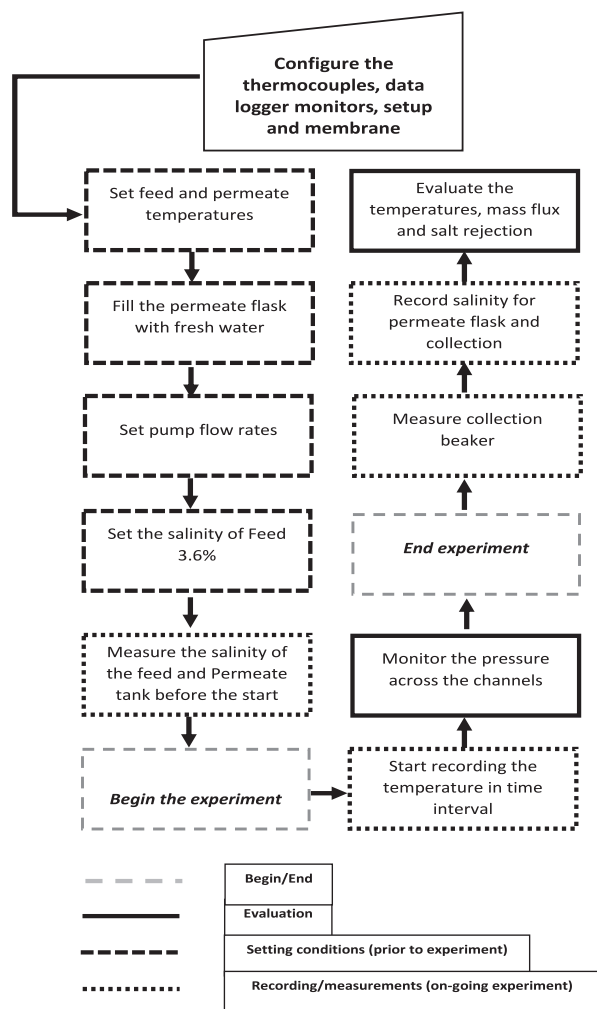

Fig. 8. Procedure and steps for experimental testing of the fabricated DCMD unit.
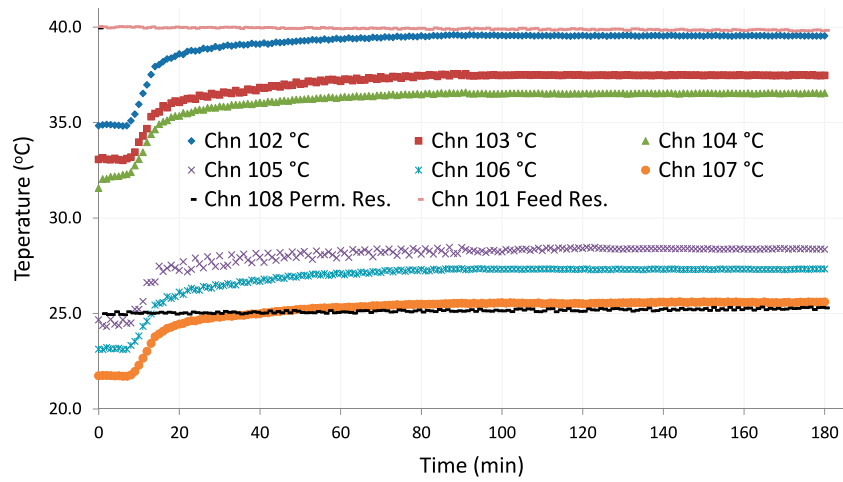
Fig. 9. Feed and permeate reservoir temperatures time evolution along with the channel walls up, middle, and downstream.
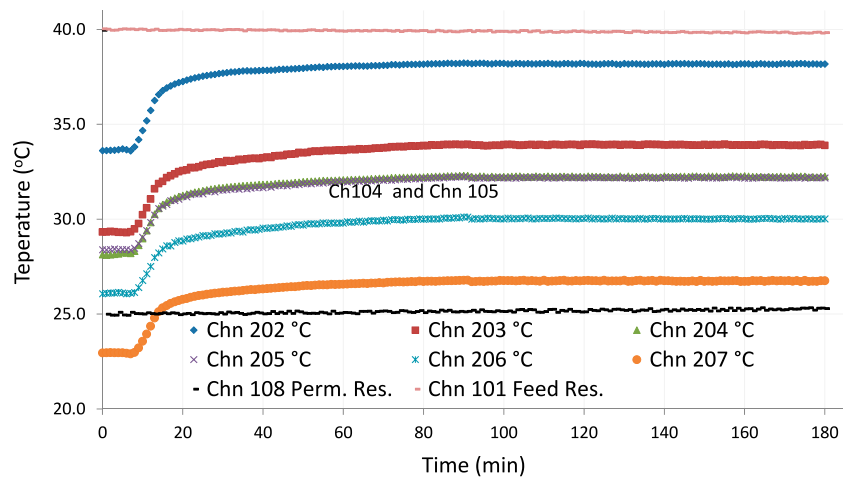

Fig. 10. Feed and permeate reservoir temperatures time evolution along with the membrane surfaces up, middle, and downstream.

Table 6
Mass flux evaluation and comparison with actual measured value

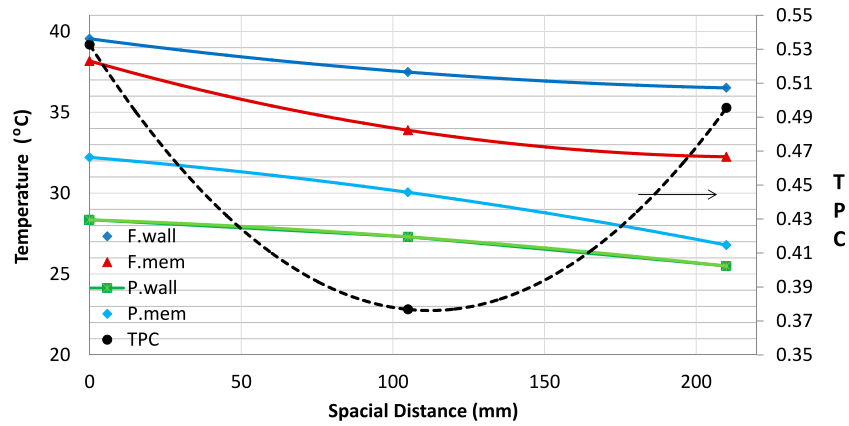| Mass flux evaluation method	Flux (kg/h m^2)	Relative error (%)
Temp.-based simulation model	6.631	14.49387492
Temp.-based experimental	7.892[a]	−1.766602192
Actual	7.633	–

[a]Three points average.

Fig. 11. Measured temperature distributions along the channel surface walls, membrane, and TPC as a function of channel length.
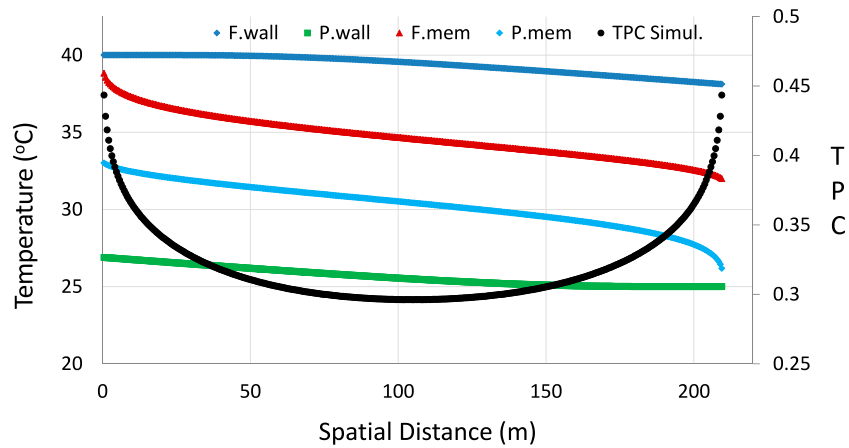

Fig. 12. Modeled temperature distributions along the channel surface walls, membrane, and TPC as a function of channel length.
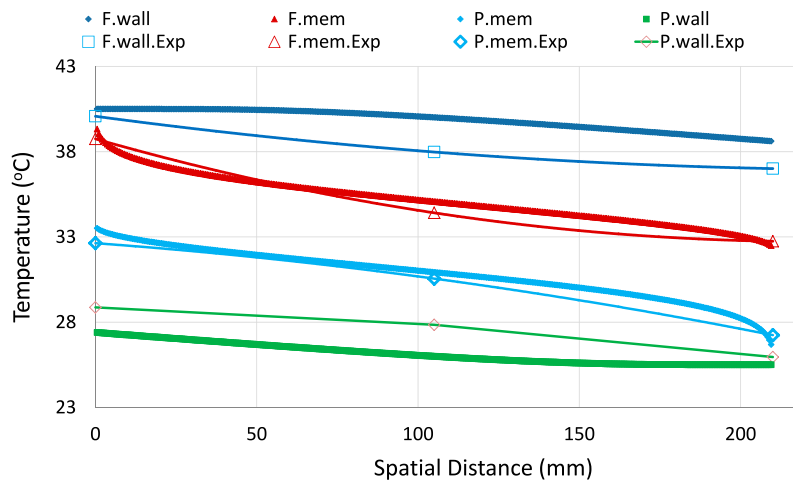

Fig. 13. Comparison of the of the measured experimental and modeled temperature data coefficient as a function of channel length.
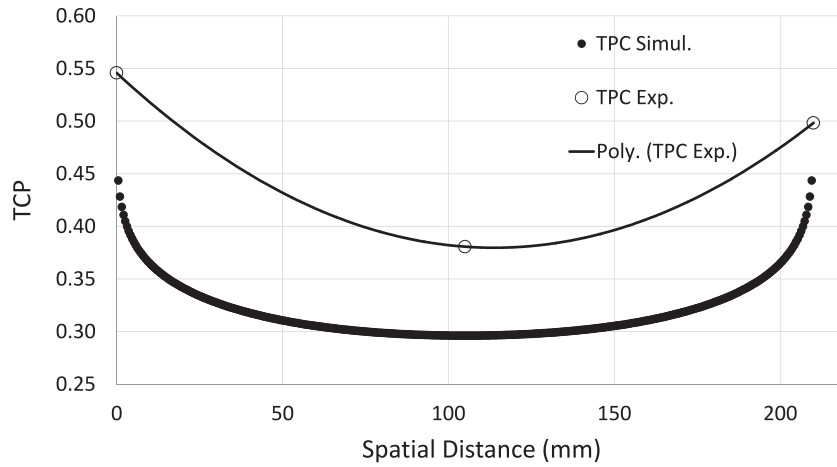
Fig. 14. Comparison of the experimentally measured and modeled TPC as a function of channel length.
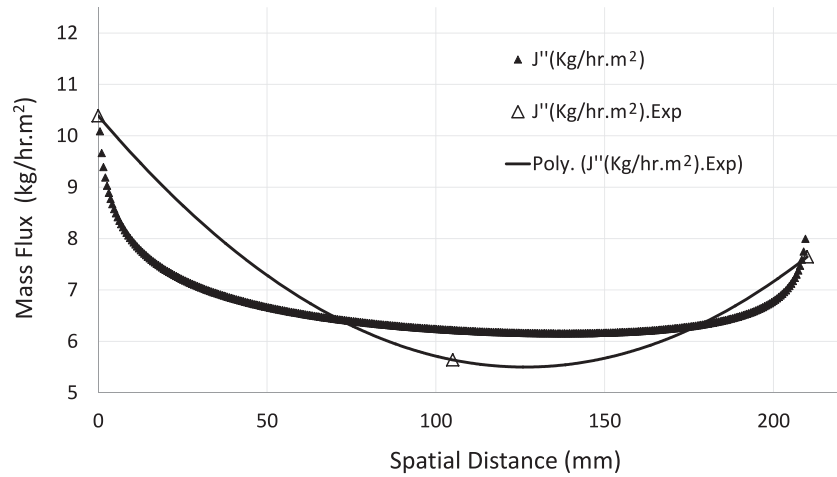

Fig. 15. Comparison of the experimentally measured and modeled mass flux as a function of channel length.
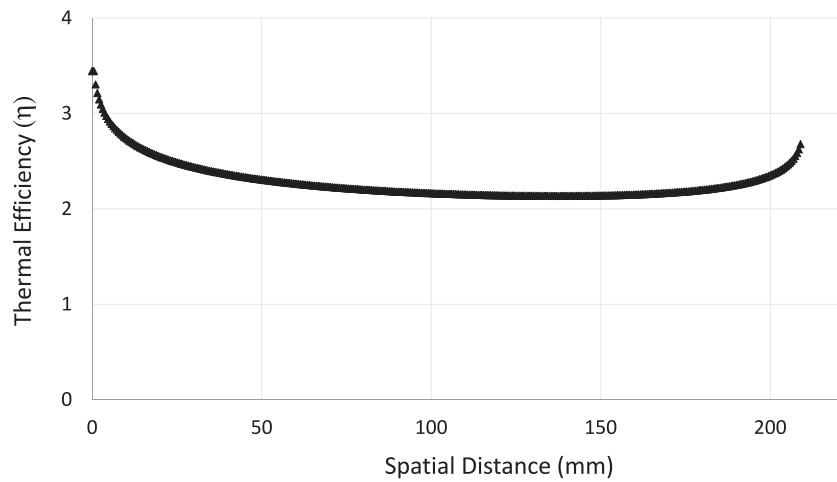

Fig. 16. Thermal efficiency of the DCMD as a function of channel length.

parameters. It provides a versatile tool that continues to be used through process development in the quest for the ultimate DCMD process metrics.

5. Conclusions

This work addressed the CFD-based modeling, simulation, and the validation of DCMD. Although the model is generic, this work has achieved model application to water desalination and the incorporation of experimental unit development. The developed simulation is applied in order to predict the spatial temperature, mass flux, and heat flux, as well as the TPC within the developed system unit. The step toward verifying the model led to building and establishing a working DCMD unit as a test bed to aid the modeling when a new innovative membrane requires further testing. The goal of this work involved the development of a validated generic flow model, enabling the investigation of the different DCMD system parameters (system configuration, membrane properties, flow material, and flow conditions) and hence quantifying their impacts on the metrics and yield of the system. This would enable the analysis to become a step closer toward having a practical working setup with the potential to aid and enhance the opportunities for commercialization of the application of DCMD units for desalination.

Theoretical modeling involves the development of suitable transport models along with heat and mass transfer modules. The two-dimensional simulation model was developed based on the Navier–Stokes equation coupled with a conjugated heat transfer problem. The outcomes aided in evaluating the flow metrics such as spatial temperature, TPC, mass flux, and thermal efficiency. As for the experimental testing, the design and fabrication process was discussed in detail. Moreover, tests were run mimicking the simulation conditions to verify and gain confidence into the working mechanism of the system. A fair agreement with low discrepancy between the model and experimental was obtained for temperature distributions, mass flux, and TPC. System metrics were obtained for the DCMD showing a suitable TPC working range (0.3–0.55), a relatively low mass flux yield (5 kg/h m^2) and low thermal efficiency (1.5%) suggesting that there are many opportunities in DCMD to enhance its overall yield.

Nomenclature

Acronyms

CFD	—	computational fluid dynamics
DCMD	—	direct contact membrane distillation
AGMD	—	air gap membrane distillation
VMD	—	vacuum membrane distillation
SGMD	—	sweep gas membrane distillation

Chemical notations

Na	—	sodium
NaCl	—	salts
H$_2$O	—	steam or liquid water

Arabic and Greek notations

x, y	—	spatial independent variable (m)
ρ	—	density (kg/m^3)
u, v	—	axial and perpendicular velocity components (m/s)
P	—	thermodynamic pressure (Pa)
G	—	gravitational acceleration
K	—	thermal conductivity (W/m K)
C_p	—	specific heat capacity (W/kg K)
T	—	temperature (T)
J''	—	mass flux (kg/m^2 h)
c_m	—	total mass transfer coefficient
P_f^{sat}	—	saturation pressure of the water at the feed side (Pa)
P_p^{sat}	—	saturation pressure of the water at the permeate side (Pa)
c_k	—	Knudson mass transfer coefficient (dimensionless)
c_p	—	Poiseuille mass transfer coefficient (dimensionless)
S_h	—	the source heat term associated with the energy equation
k, k_g, k_b	—	thermal conductivity and g and b signifies the vapor and bulk (W/m K)
$\alpha(T)$	—	Knudson temperature dependency factor (dimensionless)
$\beta(T)$	—	Poiseuille temperature dependency factor (dimensionless)
ε	—	porosity (dimensionless)
r_p	—	average pour radius (nm)
τ	—	tortuosity (dimensionless)
δ_m	—	membrane thickness (μm)
R	—	universal gas constant (J/mol K)
M_w	—	water molecular weight
P_m	—	average thermodynamic pressure across the membrane (Pa)
T_m	—	average temperature across the membrane (T)
μ	—	molecular viscosity (pa s)

ΔH	—	change in the enthalpy (J/kg K)
$H_{m,f}$	—	enthalpy of the feed water side of the membrane (J/kg K)
$H_{m,p}$	—	enthalpy of the permeate water side of the membrane (J/kg K)
Q_v, Q_c	—	latent heat of vaporization and conductive heat flux (J/kg K)
$T_{m,p}, T_{m,f}$	—	permeate membrane surface temperature and feed membrane surface temperature (T)

References

[1] M. Papapetrou, M. Wieghaus, C. Biercamp, Roadmap for the development of desalination powered by renewable energy, Promotion of Renewable Energy for Water Production through Desalination, Fraunhofer Verlag, 79S, 2010. Available from: <http://publica.fraunhofer.de/dokumente/N-137591.html>.

[2] R.B. Saffarini, E.K. Summers, H.A. Arafat, J.H. Lienhard V, Technical evaluation of stand-alone solar powered membrane distillation systems, Desalination 286 (2012) 332–341.

[3] R.B. Saffarini, E.K. Summers, H.A. Arafat, J.H. Lienhard V, Economic evaluation of stand-alone solar powered membrane distillation systems, Desalination 299 (2012) 55–62.

[4] M. Khayet, Membranes and theoretical modeling of membrane distillation: A review, Adv. Colloid Interface Sci. 164(1–2) (2011) 56–88.

[5] L.F. Greenlee, D.F. Lawler, B.D. Freeman, B. Marrot, P. Moulin, Reverse osmosis desalination: Water sources, technology, and today's challenges, Water Resour. 43 (9) (2009) 2317–2348.

[6] K.W. Lawson, D.R. Lloyd, Membrane distillation. II. Direct contact MD, J. Membr. Sci. 120(1) (1996) 123–133.

[7] T.C. Chen, C.D. Ho, Immediate assisted solar direct contact membrane distillation in saline water desalination, J. Membr. Sci. 358(1–2) (2010) 122–130.

[8] M. Asghari, A. Haradizadeh, M.Dehghani, H. Harami, Persian Gulf desalination using air gap membrane desalination: Numerical simulation and theroretical study, Desalination 374 (2015) 92–100

[9] A. Bahmanyar, M. Asghari, N. Khoobi, Numerical simulation and theoretical study on simultaneously effects of operating parameters in direct contact membrane desalination, Chem. Eng. Process. 61 (2012) 42–50.

[10] T.C. Chen, C.D. Ho, H.M. Yeh, Theoretical modeling and experimental analysis of direct contact membrane distillation, J. Membr. Sci. 330(1–2) (2009) 279–287.

[11] A. Alkhudhiri, N. Darwish, N. Hilal, Membrane distillation: A comprehensive review, Desalination 287 (2012) 2–18.

[12] B.L. Pangarkar, S.K. Deshmukh, V.S. Sapkal, R.S. Sapkal, Review of membrane distillation process for water purification, Desalin. Water Treat. 52 (2014) (28—30) 1–2, doi: 10.1080/19443994.2014.985728.

[13] B.S. Lalia, V. Kochkodan, R. Hashaikeh, N. Hilal, A review on membrane fabrication: Structure, properties and performance relationship, Desalination 326 (2013) 77–95.

[14] F.E. Ahmed, B.S. Lalia, R. Hashaikeh, A review on electrospinning for membrane fabrication: Challenges and applications, Desalination 356 (2015) 15–30.

[15] S. Murad, I. Puri, Molecular simulations of thermal transport across interfaces: Solid–vapour and solid–solid, Mol. Simul. 38 (2012) 642–652.

[16] D.J. Evans, S. Murad, Singularity free algorithm for molecular dynamics simulation of rigid polyatomics, J. Mol. Phys. 34(2) (1977) 327–331.

[17] I. Janajreh, R. Hashaikeh, D. Suwwan, Numerical simulation of membrane desalination in a conjugated heat transfer configuration: Role of spacers, in: Proceedings International Renewable and Sustainable Energy Conference (IRSEC), Ouarzazate, Morocco, October 17–19, 2014, pp. 941–947.

[18] J. Balster, D.F. Stamatialis, M. Wessling, Membrane with integrated spacer, J. Membr. Sci. 360(1–2) (2010) 185–189.

[19] L. Martínez-Díez, M.I. Vázquez-González, F.J. Florido-Díaz, Study of membrane distillation using channel spacers, J. Membr. Sci. 144(1–2) (1998) 45–56.

[20] J. Phattaranawik, R. Jiraratananon, A.G. Fane, C. Halim, Mass flux enhancement using spacer filled channels in direct contact membrane distillation, J. Membr. Sci. 187(1–2) (2001) 193–201.

[21] I. Janajreh, D. Suwwan, Numerical simulation of direct contact membrane Desalination (DCMD): II, Int. J. Eng. Res. Innov. 6 (2014) 21–33.

[22] I. Janajreh, D. Suwwan, Numerical simulation of direct contact membrane desalination in conjugate heat transfer configuration: Role of membrane conductivity, Int. J. Sustain. Water Environ. Syst. 6(2) (2014) 81–87.

[23] I. Janajreh, D. Suwwan, F. Hassan, Flow analysis of low energy direct contact membrane desalination, Int. J. Therm. Environ. Eng. 8(2) (2014) 133–138.

[24] C.D. Ho, H. Chang, C.L. Chang, C.H. Huang, Theoretical and experimental studies of flux enhancement with roughened surface in direct contact membrane distillation desalination, J. Membr. Sci. 433 (2013) 160–166.

[25] Ó. Andrjesdóttir, C.L. Ong, M. Nabavi, S. Paredes, A.S.G. Khalil, B. Michel, D. Poulikakos, An experimentally optimized model for heat and mass transfer in direct contact membrane distillation, Int. J. Heat Mass Transf. 66 (2013) 855–867.

[26] M. Bhattacharya, S.K. Dutta, J. Sikder, M.K. Mandal, Computational and experimental study of chromium (VI) removal in direct contact membrane distillation, J. Membr. Sci. 450 (2014) 447–456.

[27] K. Charfi, M. Khayet, M.J. Safi, Numerical simulation and experimental studies on heat and mass transfer using sweeping gas membrane distillation, Desalination 259(1–3) (2010) 84–96.

[28] T.Y. Cath, V.D. Adams, A.E. Childress, Experimental study of desalination using direct contact membrane distillation: A new approach to flux enhancement, J. Membr. Sci. 228(1) (2004) 5–16.

[29] Y.M. Manawi, M. Khraisheh, A.K. Fard, F. Benyahia, S. Adham, Effect of operational parameters on distillate flux in direct contact membrane distillation (DCMD): Comparison between experimental and model predicted performance, Desalination 336 (2014) 110–120.

[30] Z. Ding, L. Liu, M.S. El-Bourawi, R. Ma, Analysis of a solar-powered membrane distillation system, Desalination 172(1) (2005) 27–40.

[31] V.A. Bui, L.T.T. Vu, M.H. Nguyen, Modelling the simultaneous heat and mass transfer of direct contact membrane distillation in hollow fibre modules, J. Membr. Sci. 353(1–2) (2010) 85–93.

[32] A.O. Imdakm, T. Matsuura, Simulation of heat and mass transfer in direct contact membrane distillation (MD): The effect of membrane physical properties, J. Membr. Sci. 262(1–2) (2005) 117–128.

[33] C.L. Yaws, H.-C. Yang, To estimate vapor pressure easily. Antoine coefficients relate vapor pressure to temperature for almost 700 major organic compounds, Hydrocarbon Process. 68(10) (1989) 65–68.

[34] P. Termpiyakul, R. Jiraratananon, S. Srisurichan, Heat and mass transfer characteristics of a direct contact membrane distillation process for desalination, Desalination 177(1–3) (2005) 133–141.

[35] B.S. Lalia, E. Guillen-Burrieza, H.A. Arafat, R. Hashaikeh, Fabrication and characterization of polyvinylidenefluoride-co-hexafluoropropylene (PVDF-HFP) electrospun membranes for direct contact membrane distillation, J. Membr. Sci. 428 (2013) 104–115.

[36] J.M.O.D. Záarate, A. Velázquez, L. Peña, J.I. Mengual, Influence of temperature polarization on separation by membrane distillation, Sep. Sci. Technol. 28(7) (1993) 1421–1436.

[37] M.E. Haq, M. Shakaib, I. Ahmed, Unsteady fluid flow temperature patterns in membrane distillation process, in: Proceedings of the 13th Asian Congress of Fluid Mechanics, Dhaka, Bangladesh, 2010.

[38] L. Martínez-Díez, M.I. Vázquez-González, Temperature and concentration polarization in membrane distillation of aqueous salt solutions, J. Membr. Sci. 156(2) (1999) 265–273.